

## **Assessment of Electromagnetic Stirrer Agitated Liquid Metal Flows by Dynamic Neutron Radiography**

Scepanskis, M.; Sarma, M.; Vontobel, P.; Trtik, P.; Thomsen, K.; Jakovics, A.; Beinerts, T.;

Originally published:

January 2017

**Metallurgical and Materials Transactions B 48(2017)2, 1045-1054**

DOI: <https://doi.org/10.1007/s11663-016-0902-8>

Perma-Link to Publication Repository of HZDR:

<https://www.hzdr.de/publications/Publ-24976>

Release of the secondary publication  
on the basis of the German Copyright Law § 38 Section 4.

# Assessment of Electromagnetic Stirrers Agitated Liquid Metal Flows by Dynamic Neutron Radiography

MIHAILS ŠČEPANSKIS\*, MĀRTIŅŠ SARMA, PETER VONTOBEL, PAVEL TRTIK, KNUD THOMSEN, ANDRIS JAKOVIČS, and TOMS BEINERTS

This paper presents qualitative and quantitative characterization of two-phase liquid metal flows agitated by the stirrer on rotating permanent magnets. The stirrer was designed to fulfil various eddy flows, which may have different rate of solid particle entrapment from the liquid surface and their homogenization. The flow was characterized by visualization of the tailored tracer particles by means of the dynamic neutron radiography, an experimental method well suited for liquid metal flows due to low opacity of some metals for neutrons. The rather high temporal resolution of the image acquisition (32 Hz image acquisition rate) allows for the quantitative investigation of the flows up to 30 cm/s using neutron Particle Image Velocimetry (PIV). In situ visualization of the two-phase liquid metal flow is also demonstrated.

## I. INTRODUCTION

Despite age-old roots there is still demand and room for improvements in metallurgical processing. Energy efficiency and purity constraints are current drivers. Heating, melting and stirring of liquid metal by means of electromagnetic fields produced by alternating current is state of the art. Generally, the electromagnetically induced liquid metal flows forms a class of turbulent flows, which can be characterized by multi-vortical structure with intense fluctuations between them. These fluctuations are responsible for heat and mass transfer<sup>[1,2]</sup> and, therefore, are subject of clear industrial interest. The potential for optimization here is strongly coupled to advances in numerical modelling of the mentioned processes. There has been a significant progress in numerical modeling of the flows, such as Large Eddy Simulation performed for induction crucible and channel furnaces<sup>[1,3,4]</sup>, however these simulation lack the validation/disvalidation based on an effective non-invasive experimental method. Developing a benchmark system, which allows the comparison of simulations and experimental observations for relevant conditions of an induction stirrer of a furnace, is thus a pressing task that will ultimately allow for the tuning of numerical models.

The invasive experimental study of single-phase flow dates back to the 1970s<sup>[5,6]</sup>, and there has been steady improvement in the available probes and methods since then<sup>[1,3]</sup>. The Doppler shift method as a non-invasive tool is known from late 1980s<sup>[7]</sup>, however, it has significant limitation in spatial resolution. Recently, the new Inductive Flow Tomography method was presented<sup>[8,9]</sup>. This method has high temporal and spatial resolution, however, it is based on numerical reconstruction of the flow and requests to know conductivity of the liquid and assumes its homogeneity. Such procedure may induce some additional error in case of two-phase flow or some impurities.

Results for two-phase systems have been much more scarce<sup>[10,11]</sup>. While some limited experimental information can be obtained from X-Ray radiography methods<sup>[12-15]</sup>, these hit a fundamental limit given by the opacity of the investigated metallic melts.

Contrary to X-rays, neutrons interact with nuclei and therefore the elemental cross-section for neutron does not scale with the atomic number. Thanks to the low neutron attenuation of several metallic elements (Fig. 1), it is possible to investigate novel and more representative geometrical arrangements. The first known neutron radiography of a two-phase liquid metal flow was performed by Takenaka et al.<sup>[16]</sup>, who visualized natural and forced convection in liquid metal using tracer particles of high contrast. Later, Saito et al. studied rising gas bubbles in Pb-Bi eutectic with neutrons<sup>[17,18]</sup>. However, the flows were, initiated only by the rising bubbles without electromagnetic stirring. Therefore, the intensity of the flow was low in both mentioned neutron radiography investigations. So, the challenge to adopt the method for complex intensive flows of fundamental and industrial interest had still remained opened.

---

\* the corresponding author

MIHAILS ŠČEPANSKIS and ANDRIS JAKOVIČS are senior researchers, Laboratory of Mathematical Modelling for Environmental and Technological Processes, Department of Physics, University of Latvia, Zelju iela 25, Rīga, LV-1002 Latvia, {mihails.scepanskis, andris.jakovics}@lu.lv

MĀRTIŅŠ SARMA is a PhD student, Institute of Fluid Dynamics, Helmholtz-Zentrum Dresden-Rossendorf, 01328 Dresden, Germany, m.sarma@hzdr.de

PETER VONTOBEL, PAVEL TRTIK and KNUD THOMSEN are scientists, Paul Scherrer Institut, 5232 Villigen PSI, Switzerland, {peter.vontobel, pavel.trtik, knud.thomsen}@psi.ch

TOMS BEINERTS is a researcher, Institute of Physics, University of Latvia, Salaspils, LV-2169 Latvia, toms.beinerts@lu.lv

42 In 2014, the authors of this paper pursued the neutron radiography experiments in order to make it suitable for  
 43 investigation of intensive magnetohydrodynamic (MHD) flows<sup>[19]</sup>. The imaging equipment and quality of tracer particles  
 44 at that experiment was not enough to match the defined goal completely. Nevertheless, it was demonstrated possibility  
 45 to derive the time-averaged distribution of particle concentration and characteristic velocity of the inclusions for  
 46 experiments with wide range of stirring intensity<sup>[20]</sup>. The experiment was repeated using the same set-up, but improved  
 47 particles and new high speed camera. Thus, current work concentrates on refinements and obtaining quantitative results  
 48 for the flow of electromagnetically agitated liquid metal with solid inclusions.

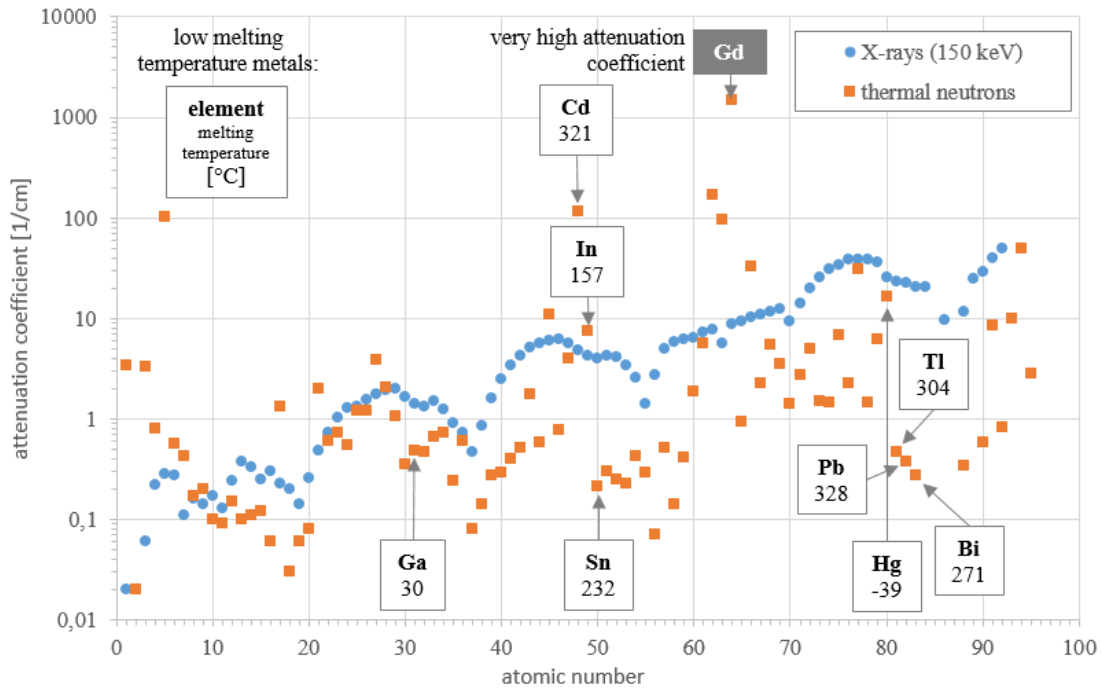
## 49 II. NEUTRON RADIOGRAPHY METHOD

### 50 II.1. Neutron imaging

51 Fig. 1 shows the difference in attenuation coefficients for neutron and X-rays, respectively. Transmission of the initial  
 52 beam can be calculated (both for X-rays and neutrons) according to the Beer-Lambert law:

$$53 \quad I = I_0 e^{-\alpha_{N,X} d}, \quad (1)$$

54 where  $d$  is the thickness of a sample in the beam direction;  $I$  and  $I_0$  denote the intensity of the beam after and before  
 55 passing the sample;  $\alpha$  is the attenuation coefficient for neutrons (subindex  $N$ ) and X-rays (subindex  $X$ ).



56  
 57 Fig. 1 – attenuation coefficients for X-rays (150 keV) and thermal neutrons for different atoms.

58 The present experiment was performed at the spallation neutron source SINQ, [NEUTRA](#) instrument. The  
 59 characteristics of the NEUTRA beamline can be found in ref. [21]. The proton current throughout the experiments was  
 60 about 1.46 mA leading to average neutron flux of  $1.6 \cdot 10^7$  n/cm<sup>2</sup>/s.

61 The experiments were performed at measuring position 2 (the ration of the distance from the aperture to the diameter  
 62 of the collimator exit  $L/D$  is equal to 375) and the “standard” MIDI-camera box was utilised. A 200  $\mu$ m thick <sup>6</sup>LiF/ZnS  
 63 scintillator screen was used. A sCMOS camera detector (Andor Neo, pixel size 6.5 micrometres) together with a Nikon  
 64 lens, AF-S NIKKOR 50mm 1:1.4G was used throughout the experiments. In order to achieve as high spatial resolution  
 65 as possible the sample of liquid metal was placed close to the scintillator screen. The mean distance between the liquid  
 66 metal sample and the scintillator screen was about 1.5 cm.

### 67 II.2. Model liquid

68 As the dynamic neutron imaging is a transmission type of experiment, it is essential to select a model liquid as  
 69 transparent for neutrons as possible. Another restriction is the melting temperature of the model liquid as it is less  
 70 complicated to perform the experiment in a low temperature environment. Low temperature metallic elements are

71 highlighted on Fig. 1 (melting temperature is also mentioned on the figure). Gallium (Ga) was chosen as working liquid  
72 among the highlighted elements because of relatively small absorption coefficient and low melting temperature.

### 73 II.3. Particles

74 The tracer particles have to fulfil various requirements to be efficiently used for neutron radiography purposes, but  
75 chiefly they have to possess as high contrast as possible to the model liquid. Gadolinium oxide ( $Gd_2O_3$ ) is a good  
76 solution since it does not have ferromagnetic properties, is available in form of powder and Gadolinium is the stable  
77 element of the highest neutron cross-section.

78 Another requirement on the particles is their density. Generally, the desired density may depend on a goal of an  
79 experiment. E.g., if specific inclusions are simulated, than the target density can be that to keep an inclusions-to-liquid  
80 density ratio same as in the simulation. We created the particles for neutron visualization as mixture of three  
81 components: gadolinium oxide, lead powder and glue (6%  $Gd_2O_3$  - 10% glue - 84% Pb, mass %). Such particles are  
82 supposed to be the same density as that of gallium. However, by changing the mixing ratios the particle densities can be  
83 easily tailored depending on the experimental goal.

84 Particle size is another essential property to be considered. It is restricted by the available spatial resolution of the  
85 imaging device from one side and should satisfy goals of the experiments from the other side. For flow investigation it is  
86 good to use small particles, which behave as flow tracers. However, the goals of experiments may differ and some  
87 inertia particles of bigger size may be requested. We milled and sifted the hardened glue mixture out for the specific  
88 fraction. About  $0.3 \pm 0.1$  mm particles were used for the present experiment.

## 89 III. EXPERIMENTAL SET-UP

90 Unfortunately, there is no way to use real scale metallurgical equipment for neutron experiments due to obvious  
91 limitations e.g. neutron transmission, so a special scaled-down experimental set-up was designed.

92 First of all, the width of the vessel is limited by the width of the neutron beam. Consequently, we decided to limit the  
93 experimental vessel with 10 x 10 cm perpendicular to the beam. The third dimension of the vessel with liquid metal  
94 should be optimized with respect to the beam attenuation by the liquid metal. E.g., according to the expression (1), 3 cm  
95 gallium will leave 23% of the initial intensity of the beam.

96 Even though 3D imaging of dynamic systems can be performed<sup>[22]</sup>, due to the very high temporal resolution  
97 necessary for the visualization of the liquid metal flow only 2D imaging is realistically possible. It means, first of all,  
98 that it is necessary to avoid presence of materials of high attenuation coefficient in a way of the neutron beam. Then, it is  
99 desirable to agitate the quasi-2D flow, which will be relevant to certain cross-section of a real flow in studied equipment.  
100 These requirements are fulfilled by using rotating permanent magnet technology in the present experiment. Generally,  
101 since significant reduction of prices for permanent magnets the moving (usually rotating) permanent magnet technology  
102 became an efficient alternative for AC stirrers last decade. There is no resistivity loss in such systems, an alternating  
103 magnetic field is created by rotating permanent magnets<sup>[23,24]</sup>. The solenoidal inductor like in the induction crucible  
104 furnace can be replaced by two pairs of counter-rotating permanent magnets at the sides of the vessel. Ščepanskis et al.  
105 demonstrated numerically principal similarity of the flow agitated in such system to that of the induction crucible  
106 furnace<sup>[25]</sup>

107 The scheme of active zone of the set-up is shown on Fig. 2. Tab. 1 contains dimensions of the system and remanence  
108  $B_r$  of the radially magnetized Nd-Fe-B magnets. It can be recognized in Fig. 2 (b) that there are no parts of the set-up in  
109 the perpendicular direction to the rectangular vessel for liquid metal. This principle of design is essential in order to  
110 avoid beam weakening. The vessel is produced from window glass, which does not contain any neutron opaque  
111 elements and does not chemically react with gallium.

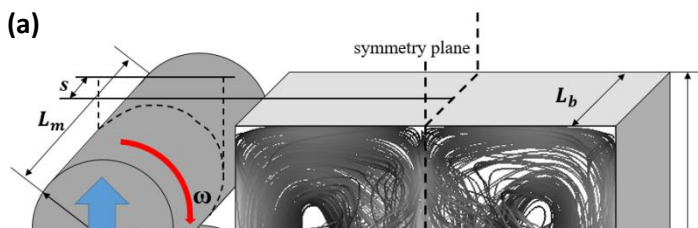
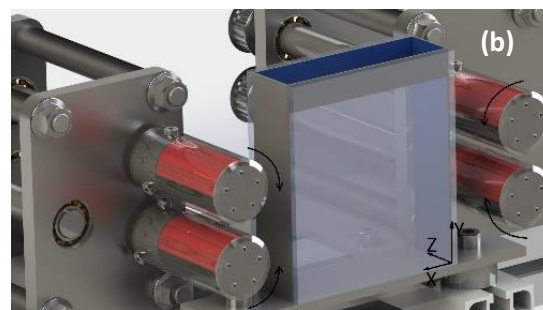


Fig. 2 – Design of a rectangular permanent magnet stirrer: (a) the drawing and the illustration of the flow pattern; (b) 3D rendering of the active part of the set-up.



112 The mechanical part of the set-up (not shown in Fig. 2) consists of a pair of blocks for magnet shafts with belt  
113 pulleys on the opposite side of the magnets, a frame with a motor and driving elements, a system of gears and pulleys.  
114 For a drawing and an image of the full system see Ščepanskis et al.<sup>[19]</sup>. The mechanical system is designed to fulfil  
115 several schemes of magnets rotation with minimal transformations. These combinations of rotation ensure different  
116 types of flow, which will be described in the results section.

117 The set-up does not contain a heater. It was observed that small amount of heat, which is generated in the liquid in  
118 induction way is enough to raise temperature for few degrees from a room temperature to keep gallium liquid.  
119 Moreover, it was observed that gallium can be slightly overcooled between experiments still keeping it melted.

120

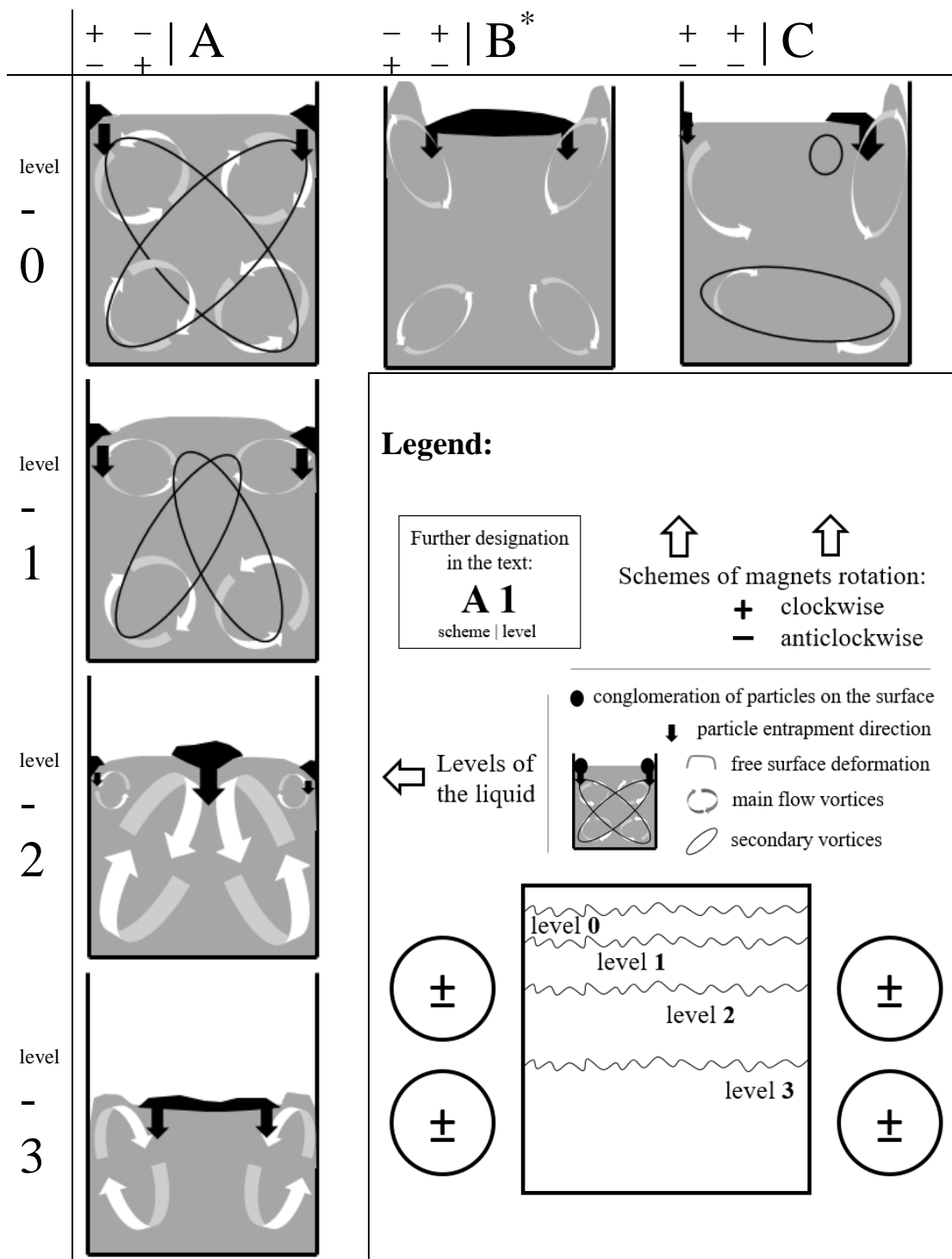
## IV. RESULTS

121

### IV.1. Visualization of different stirring regimes

122 As it was already mentioned, the set-up was designed to fulfil several types of liquid movement by different rotation  
123 of magnets. Fig. 3 schematically demonstrates the flow patterns induced by different types of magnet rotation. Fig. 4-6  
124 show examples of neutron images in different flow configurations and for different magnet rotation speeds.  
125 Corresponding videos are available in the supplemental online resource.

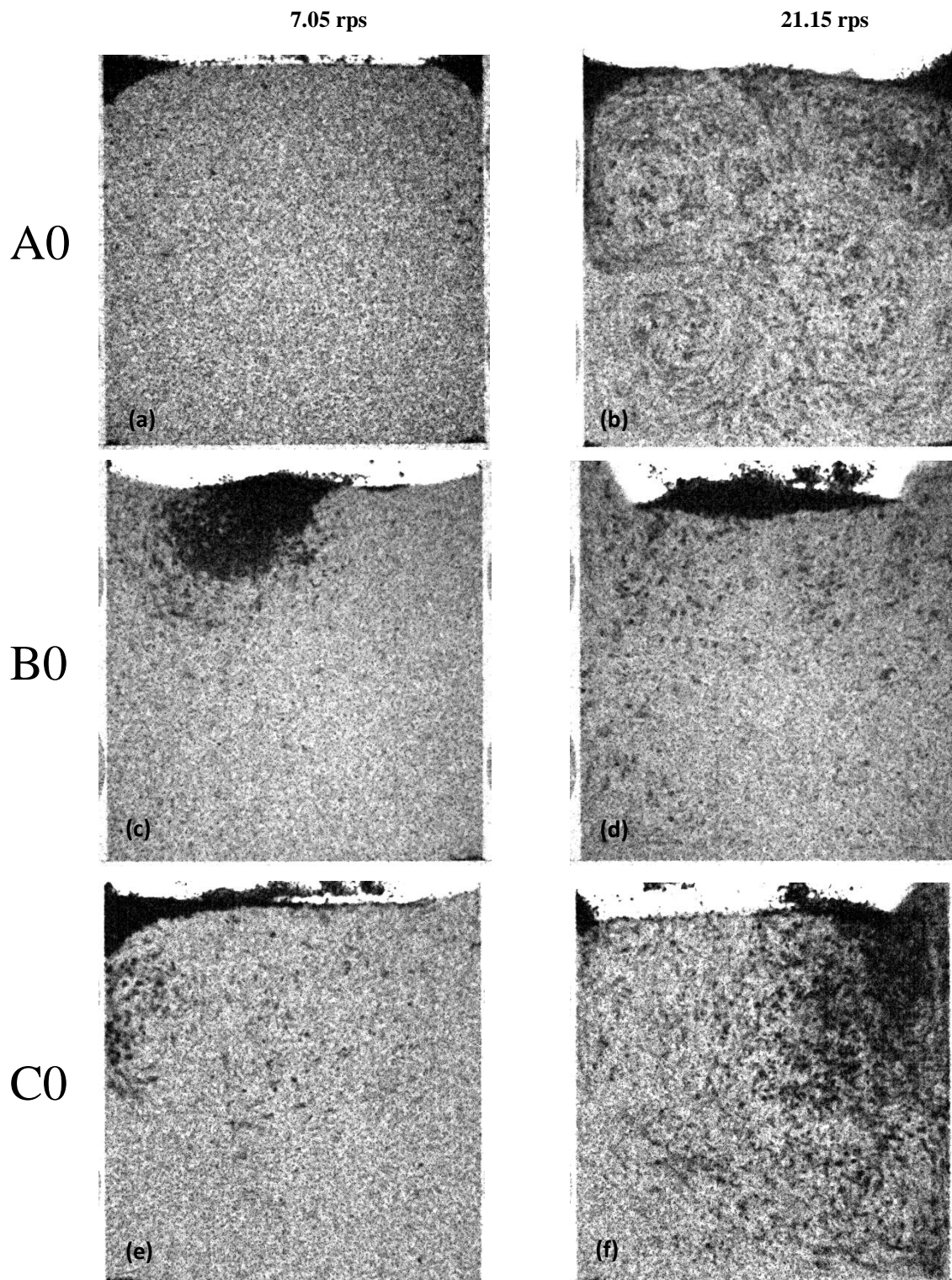
126 The basic A0 configuration contains four counter-rotating vortices; each of them is generated at the wall by the  
127 proper magnet rotation. This configuration generally corresponds to the toroidal vortices observed in a cross-section of  
128 an induction crucible furnace and is wide-spread in metallurgy. However, due to highly turbulent nature of the flow,  
129 such structure is unstable. The four vortices pattern frequently transforms into three eddies, the diagonal vortex can be  
130 observed in this flow for short time period. Flow transformation into three-eddy structure plays significant role for  
131 inclusions homogenization between the upper and lower eddies. The first row in Fig. 4 shows that a number of particles  
132 involved in motion strongly increases with increase of magnet rotation speed.



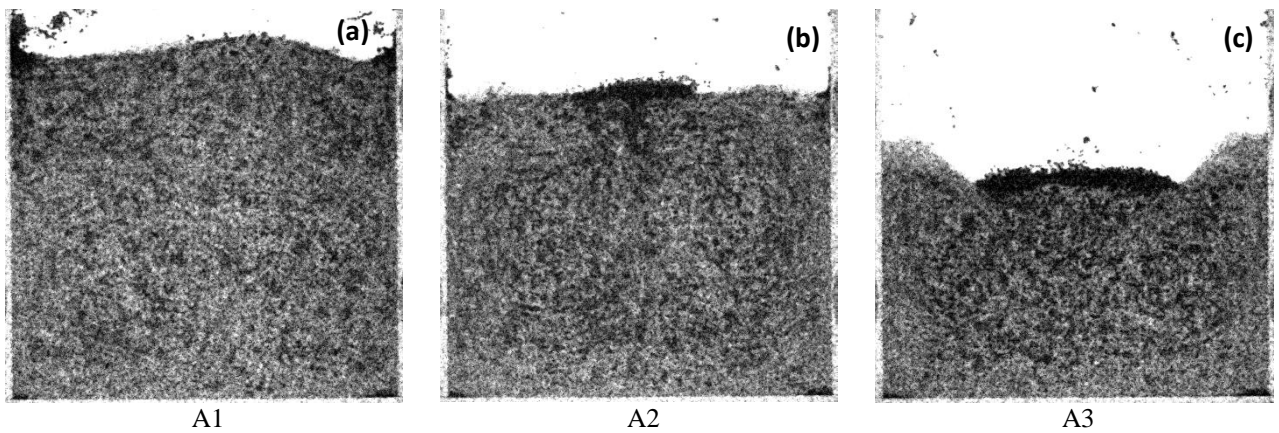
133  
134

Fig. 3 - The summary of different flow patterns as the result of different magnet rotation schemes.

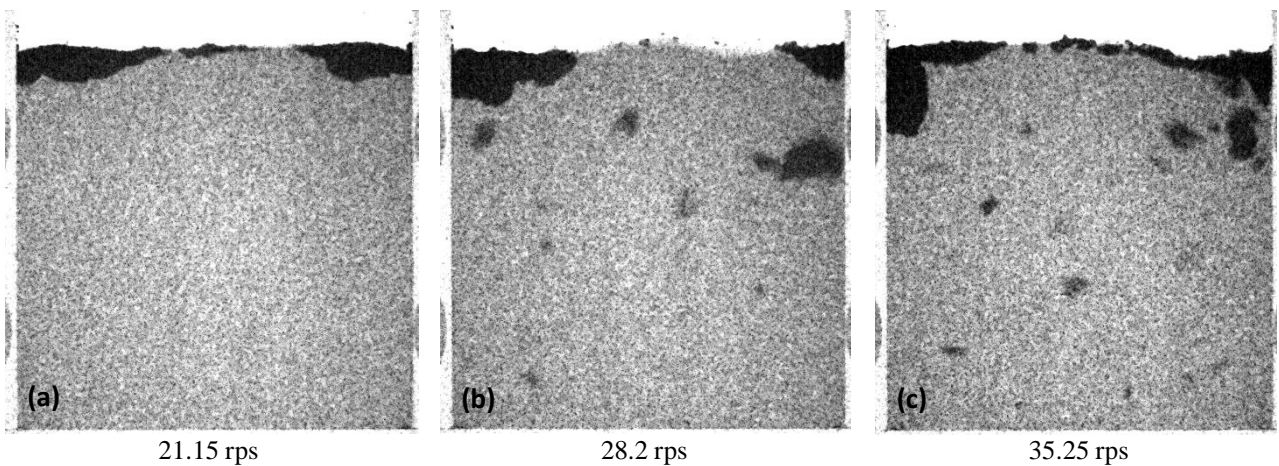
\* The flow, which is related to magnet rotation scheme is fundamentally the same like in the scheme B, but symmetric in respect to a vertical plane. Therefore, such rotation scheme is not considered here.



135 Fig. 4 - Snapshots of neutron radiography visualization of the different type MHD flow (see designation in Tab. 2) at two different  
 136 magnet rotation speeds: 7.05 rps and 21.15 rps.  
 137



138 Fig. 5 - Snapshots of neutron radiography visualization of the flow at different liquid levels (see designation in Tab. 2), magnet  
 139 rotation speed 21.15 rps.



140 Fig. 6 - Snapshots of neutron radiography visualization of non-wetted particles in the A0 case (see designation in Tab. 2) for different  
 141 magnet rotation speed.

142 The flow pattern changes by decreasing the liquid level (Fig 5). Since the upper pair of magnets influence less  
 143 volume of liquid metal, the upper vortices become smaller. With minor decrease of the level (A1) the flow pattern  
 144 generally remains the same, but the short term diagonal vortex is not observed any more, elongation of lower eddies can  
 145 be shortly recognized, like it is shown in Fig. 3. With further level lowering (A2) the elongated secondary eddies  
 146 become a main flow pattern with tiny rudimentary upper vortices in the corners. Finally, when the liquid level reaches  
 147 the middle line between the upper and the lower magnets, it is observed only the two vortices structure with wide  
 148 stagnation zone between them.

149 Fig. 4 demonstrates that increasing magnet rotation speed not only increases a number of admixed particles, but also  
 150 slightly changes the flow pattern. In case of symmetric configuration B0 sensitivity to asymmetric particle distribution is  
 151 decreased by intensification of stirring. In the case C0, higher stirring rate significantly increases the surface deformation  
 152 and shifts dominated particle entrapment zone.

153 Figures. 4-5 demonstrate behavior of the particles, which were carefully wetted by the liquid metal. Such wetting  
 154 resulted, in fact, in particles coating with liquid gallium. The procedure was necessary to overcome natural non-  
 155 wettability of many materials, including that of the particles, in liquid metal. The particles were separated by liquid film  
 156 to avoid clustering and to favor their entrapment into the flow. Fig. 6 demonstrates the case of non-wetted particles.  
 157 Relatively high 21.15 rps magnet rotation speed is not enough to overcome surface tension and admix the particles. With  
 158 increase of magnet rotation speed (see 28.2 rps and 35.25 rps in Fig. 6) flow intensity become enough to involve several  
 159 clusters in the motion. However, surface tension of such clusters of the non-wetted particles is so strong that it is almost  
 160 impossible to break them by flow pulsations within limits of reasonable stirring rates. Nevertheless, the case of non-  
 161 wetted particles seems to be important since it nicely simulates slag entrapment process in many metallurgical  
 162 applications.

#### IV.2. PIV and PTV processing of the neutron images

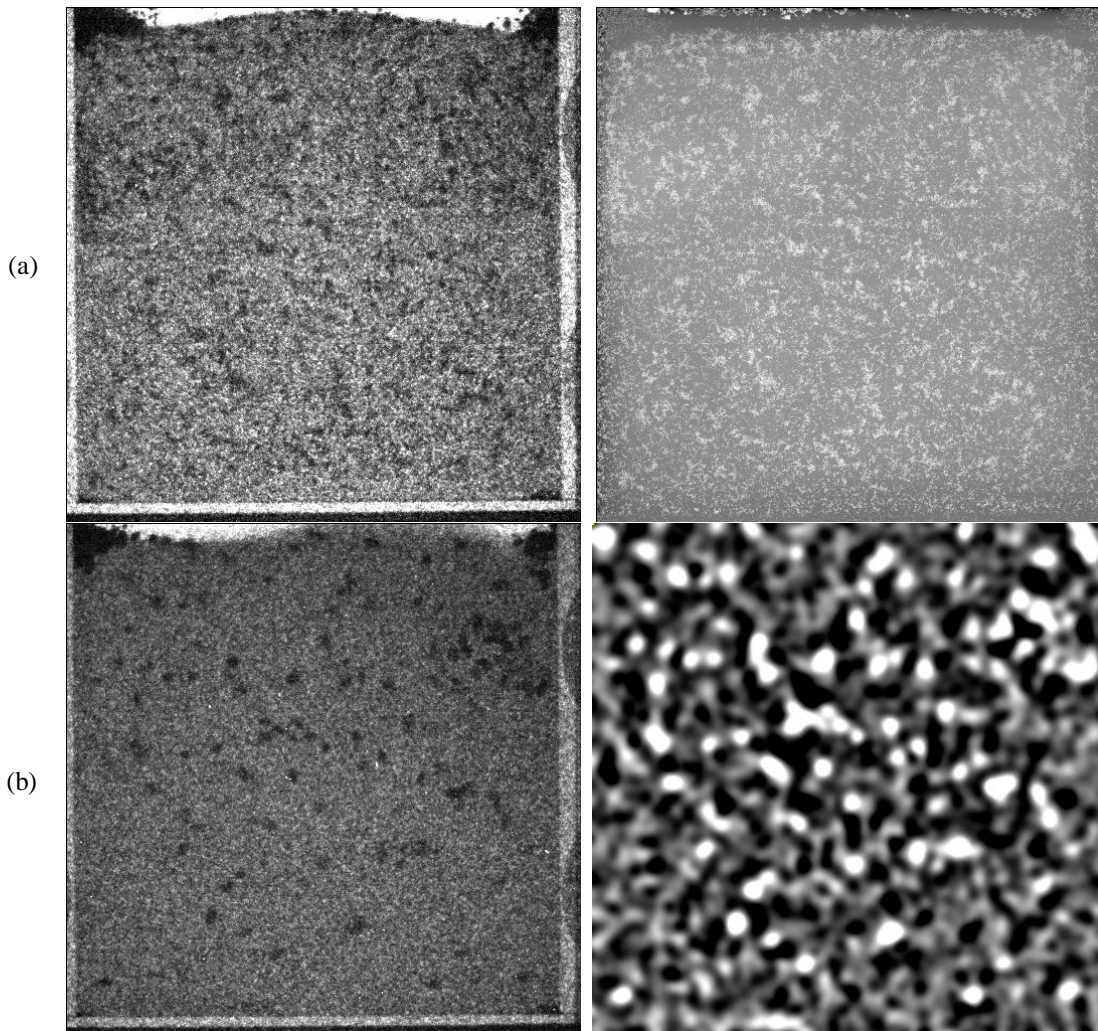
Generally, one can identify three possible methods corresponding to density of spatial distribution of particles in the images – particle tracking velocimetry (PTV) for low density, particle image velocimetry (PIV) for medium density and speckle velocimetry for high density. However, the high particle-to-noise ratio is a limiting factor and blurs the boundaries between methods in this experiment. While the main objective of PIV is determination of the displacement between two patterns of grey levels and resolving particles is not necessary, then PTV directly measures particle displacement. This sets a particle size and intensity threshold for PTV much higher than for PIV.

Prior image processing was done with *ImageJ 1.50* software. Flat-field correction was applied to remove the uneven illumination and 1px sized outliers were removed to reduce the “salt-and-pepper” noise. Nevertheless, significant amount of random noise still remained; therefore, each background pixel, which deviates from the median by more than a certain value, was replaced by median intensity value of the surrounding pixels. Finally, a mean filter was used for slight smoothing.

Fig. 7 (a row) demonstrates an example of a processed image with the basic particles ( $0.3\pm 0.1$  mm). This figure clearly shows that signal intensity for a single particle is comparable with that of the noise, this fact makes it nearly impossible to apply simple particle tracking tools in this case. However, PIV processing is possible for such image.

Fig. 7 (b row) demonstrates a processed image with larger particles (diameter  $>0.4$  mm) admixed in the flow. Fig. 7 (b row, right) is subject of additional image processing with the goal to enhance visibility of the particles and reduce the random noise. Two images were subtracted and Gaussian smoothing with large and small standard deviation was applied. Then, pixel values of the resulting image are mapped in defined range.

Unfortunately, these particles have quite high size dispersion since they were sifted as the biggest fraction ( $>0.4$  mm). It can be clearly seen that the light intensity of the particles is greatly enhanced by the algorithm and, consequently, become usable for PTV processing. Nevertheless, unfortunately, we cannot determine from this image a particle size threshold for this method.



186 Fig. 7 - An example of the results of premature image processing: (a) for the basic particles ( $0.3\pm 0.1$  mm); (b) for the large  
187 ( $>0.4$  mm). The raw neutron images are shown in the left column, and the proper processed images of the liquid metal zone are shown  
188 in the right column.

189 For PIV, the *PIVview2C 3.3.2* software from *PivTec* was used to perform cross correlation of images for x- and y-  
190 velocity components. A  $16 \times 16$  px window with 8 px step was chosen. The region of interest was limited to  $10 \times 10$  cm  
191 (the size of vessel) that corresponds to  $480 \times 460$  px. The multi-grid interrogation method was used with the initial  
192 sampling window of  $96 \times 96$  px. Such routine ensures nominal spatial resolution of 0.22 mm (the pixel size of the  
193 image). Images were interpolated using the B-Spline interpolation scheme with order of 3, and peak search was done by  
194 the least squares Gauss fit. Outliers were detected, then re-evaluated with the larger sample window and replaced, if  
195 evaluation was successful. Approximately 25% from all vectors were left as outliers in the end. However, we admit that  
196 the definition of the outlier vector is currently based on a subjectively selected threshold value. Experiments to provide  
197 better understanding of the outliers are to be performed in the near future. Finally, we applied the running mean of 10  
198 frames using 5 valid vectors. The obtained velocity field is shown in Fig. 8: the example of the instant field is image (a)  
199 and time averaged results in (b).

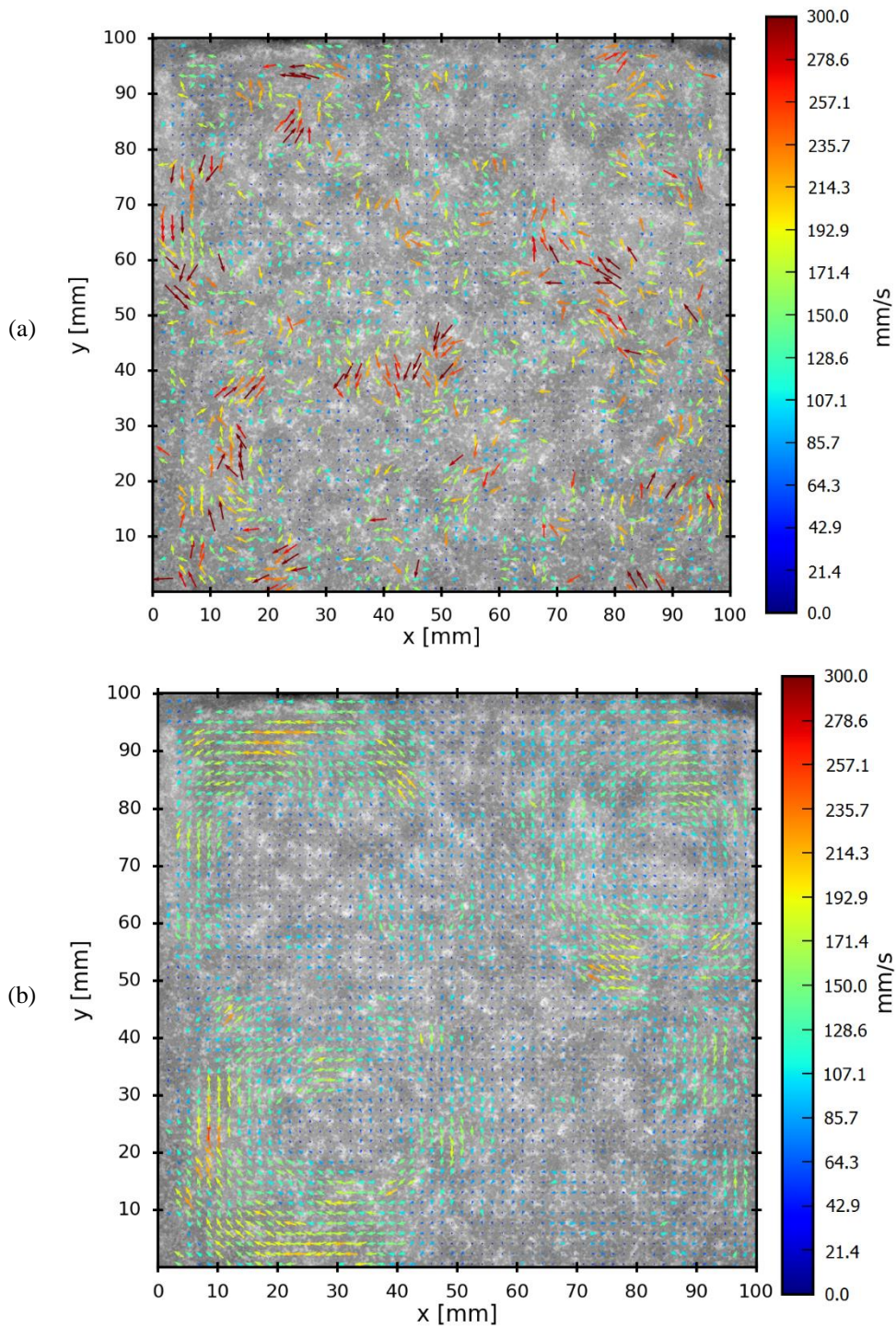
200 Instant image (Fig. 8 a) indicates presence of numerous small vortices, which appears as chaotic vectors of high  
201 magnitude since space resolution of PIV seems to be not enough to resolve them. Generally, averaging for some time  
202 period helps to visualize structure of the flow, e.g. four vortices structure can be recognized in Fig. 8 (b). Corresponding  
203 video of the PIV results is available as the Supplemented Online Resource.

204 Despite the generally satisfactory results, some problematic points of the method can be noted. Accordingly to the  
205 scheme of the flow motion (Fig. 3, A0) and as it can be seen in the video (see the Supplemented Online Resource), the  
206 near wall region next to the upper magnets is characterized with high flow intensity that leads to particle entrapment  
207 from the surface to the melt. Nevertheless, the PIV results do not show significant velocities there. It becomes clear that  
208 PIV algorithm cannot resolve particles, which are too dense in this region since they are just entrapped. Thus, we can  
209 conclude that PIV may lead to significant underestimation of flow velocity in the zones of high particle density.

210 The larger particles ( $>0.4$  mm) were used in order to demonstrate PTV post-processing of neutron images. PTV  
211 analysis was done by using *TrackMate* add-on for ImageJ software. Laplacian of Gaussian segmentation was applied to  
212 detect the particles with average spot size set to 10 px. The detected particles are shown with the circles in Fig. 9 (a).  
213 The simple Linear Assignment Problem (LAP) tracker was used to link particles in sequent snapshots. The maximum  
214 linking distance for particles was limited to 20 px as that approximately corresponds to the maximum travel distance for  
215 the particles in this flow. An example of the tracking result is presented in Fig. 9 (b).

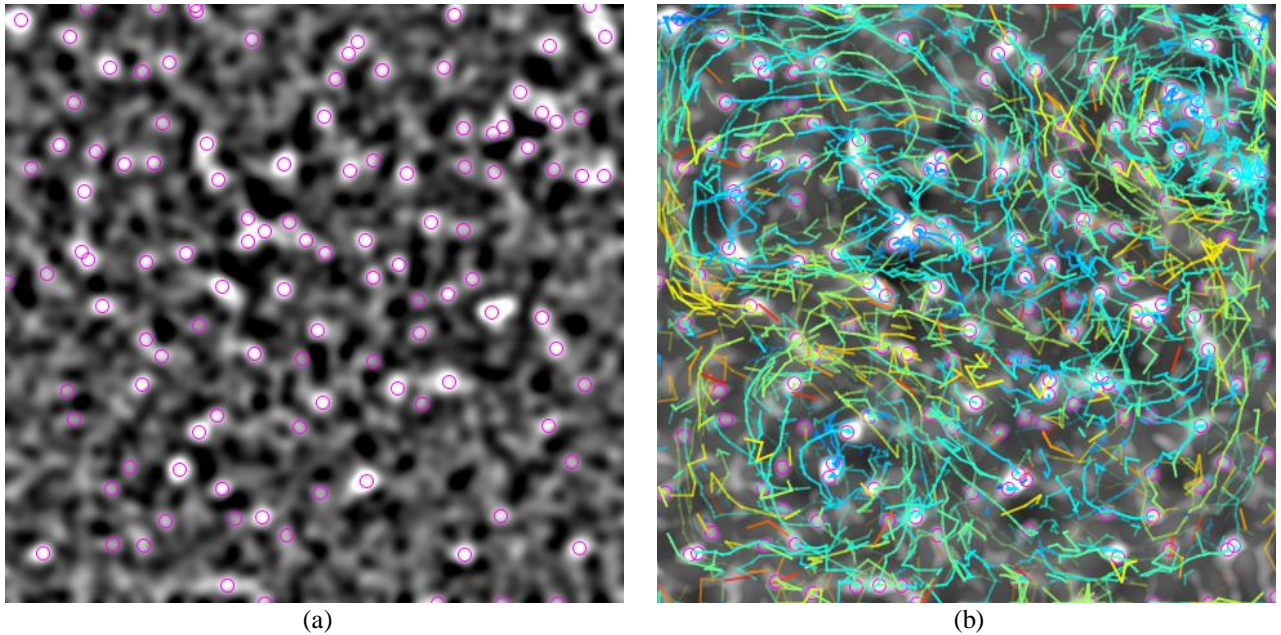
216 It should be mentioned that some artificial particles are detected in further analysis. However, we believe that better  
217 optimization of used parameters may reduce such errors; and PTV can be successfully applied if information about  
218 particle trajectory is needed.

219 Nevertheless, trajectories in Fig. 9 (b) nicely indicate 3 vortices structure that corresponds to one of the secondary  
220 vortices realization in A0 scheme (see Fig. 3).



221 Fig. 8 - Examples of neutron PIV: (a) instant capture; (b) time averaged for 10 frames (0.31 s). These PIV images corresponds to A0  
 222 rotation scheme, magnets rotation speed 28.2 rps.

223



224 Fig. 9 - An example of PTV post-processing: (a) illustration of particles identification by the algorithm (circles), the image  
 225 corresponds to prematurely processed image in Fig. 7 (b raw); (b) particles trajectories calculated by the PTV algorithm. Large  
 226 particles (>0.4 mm), A0 magnets rotation scheme, 28.2 rps.

227

## V. CONCLUSIONS

228 This paper successfully demonstrated power of the dynamic neutron radiography method to fulfill in situ  
 229 visualization of complex intense liquid metal flows relevant to metallurgical applications, particularly to induction  
 230 stirrers. The permanent magnets system is good to reproduce various flow patterns relevant to different types of stirrers.  
 231 The dynamic neutron radiography qualitatively demonstrated efficiency of particle entrapment and their  
 232 homogenizations in various eddy flows agitated at different stirring regimes. This method seems to be unique for in situ  
 233 visualization of two-phase liquid metal flows.

234 It was also demonstrated in the paper that quantitative analysis of the experimental data is possible utilizing PIV and  
 235 PTV post-processing methods. The method is able to ensure high temporal and spatial resolution simultaneously, up to  
 236 31 ms and 0.22 mm respectively (the nominal resolution of imaging) in the present paper. It was recognized that PTV  
 237 post-processing requires larger particles than PIV.

238 To the authors' best knowledge, this is the first quantitative in situ visualization of liquid metal flow of high intensity  
 239 (30 cm/s). This fact gives a credit to consider the results as a significant step towards development of a new practical  
 240 tool for experimental investigations of intense liquid metal flows, which are a key phenomenon in many metallurgical  
 241 devices and processes.

242

## SUPPLEMENTED ONLINE RESOURCE

243 The video file contains neutron radiography visualization of different types of the MHD flows described in Fig. 3,  
 244 variation in magnet rotation speed and examples of PIV and PTV post-processing.

245

## ACKNOWLEDGMENTS

246 This work was supported by European Social Fund (project. no. 2013/0018/1DP/1.1.1.2.0/13/APIA/VIAA/061) and by  
 247 the German Helmholtz Association in frame of the Helmholtz-Alliance LIMTECH. The experiment was performed at  
 248 the Swiss Spallation Neutron Source SINQ, Paul Scherrer Institute, Villigen, Switzerland. The authors also acknowledge  
 249 engineer Raimonds Nikoluškis (UL) for design and supervision during manufacturing of the setup, engineers Matīss  
 250 Kalvāns (UL) and Thomas Steinberg (LUH) for support and operation of the setup during the experiment. The authors  
 251 are thankful to Dr. Kalvis Kravalis (UL) for his effort in preparation of particles; Sten Anders and Dr. Tom Weier (both

252 HZDR) for the invaluable help with particle tracking methods; Dr. Andris Bojarevičs and Dr. Ernests Platacis (both UL)  
253 for support and ideas in set-up design and preparation.

254

## REFERENCES

- 255 1. A. Umbrashko, E. Baake, B. Nacke, A. Jakovics: *Met. Mater. Trans. B*, 2006, vol. 37B, pp. 831-838.  
256 2. M. Ščepanskis, A. Jakovičs, E. Baake, B. Nacke: *Magnetohydrodynamics*, 2012, vol. 48, pp. 677-686.  
257 3. M. Kirpo, A. Jakovičs, E. Baake, B. Nacke: *Magnetohydrodynamics*, 2007, vol. 43, pp. 161-162.  
258 4. S. Pavlovs, A. Jakovičs, E. Baake, B. Nacke, M. Kirpo: *Magnetohydrodynamics*, 2011, vol. 47, no. 4, pp. 399-412.  
259 5. C. Trakas, P. Tabeling, J. P. Chabrierie: *Journal de Mécanique Théorique et Appliquée*, 1984, vol. 3, pp. 345-370.  
260 6. D. J. Moore, J. C. R. Hunt: *Progress in Astronautics & Aeronautics*, 1983, vol. 84, pp. 359-373.  
261 7. Y. Takeda: *Nucl. Techn.*, 1987, vol. 79, pp. 120-124.  
262 8. T. Wondrak, S. Eckert, G. Gerbeth, F. Stefani, K. Timmel, A. J. Peyton, N. Terzija, W. Yin: *Steel Research Int.*, 2014, vol. 85, pp.  
263 1266-1273.  
264 9. K. Timmel, N. Shevchenko, M. Röder, M. Anderhuber, P. Gardin, S. Eckert, G. Gerbeth: *Met. Mater. Trans. B*, 2015, vol. 46, no.  
265 2, pp. 700-710.  
266 10. S. Taniguchi, J. K. Brimacombe: *ISIJ Int.*, 1994, vol. 34, pp. 722-731.  
267 11. M. Ščepanskis, A. Jakovičs, E. Baake, B. Nacke: *Int. J. Multiphase Flow*, 2014, vol. 64, pp. 19-27.  
268 12. M. Iguchi, T. Chihara, N. Takanashi, Y. Ogawa, N. Tokumitsu, Z. Morita: *ISIJ Int.*, 1995, vol. 35, pp. 1354-1361.  
269 13. V. F. Chevrier, A. W. Cramb: *Met. Mater. Trans. B*, 2000, vol. 31B, pp. 537-540.  
270 14. X. Dai, X. Yang, J. Campbell, J. Wood: *Mater. Sci. Eng. A*, 2003, vol. 354, pp. 315-325.  
271 15. W. Mirihanage, W. Xu, J. Tamayo-Ariztondo, D. Eskin, M. Garcia-Fernandez, P. Srirangam, P. Lee: *Materials Letters*, 2016, vol.  
272 164, pp. 484-487.  
273 16. N. Takenaka, T. Fujii, A. Ono, K. Sonoda, S. Tazawa, T. Nakanii: *Nondestructive Testing & Evaluation*, 1994, vol. 11, no. 2-3,  
274 pp. 107-113.  
275 17. Y. Saito, K. Mishima, Y. Tibita, T. Suzuki, M. Matsubayashi: *Appl. Radiation & Isotopes*, 2004, vol. 61, pp. 683-691.  
276 18. Y. Saito, K. Mishima, Y. Tobita, T. Suzuki, M. Matsubayashi: *Exp. Therm. Fluid Sci.*, 2005, vol. 29, no. 3, pp. 323-330.  
277 19. M. Ščepanskis, M. Sarma, R. Nikoluškins, K. Thomsen, A. Jakovičs, P. Vontobel, T. Beinerts, A. Bojarevičs, E. Platacis:  
278 *Magnetohydrodynamics*, 2015, vol. 51, pp. 257-265.  
279 20. M. Sarma, M. Ščepanskis, A. Jakovičs, K. Thomsen, R. Nikoluškins, P. Vontobel, T. Beinerts, A. Bojarevičs, E. Platacis: *Physics*  
280 *Procedia*, 2015, vol. 69, pp. 457-463.  
281 21. E. H. Lehmann, P. Vontobel, L. Wiesel: *Nondestr. Test. Eval.*, 2001, vol. 16, pp. 191-202.  
282 22. A. P. Kaestner, B. Münch, P. Trtik, L. Butler: *Opt. Eng.*, 2011, vol. 50, no. 12, p. 123201.  
283 23. A. Bojarevičs, T. Beinerts: *Magnetohydrodynamics*, 2010, vol. 46, pp. 333-338.  
284 24. T. Beinerts, I. Bucenieks, A. Bojarevičs, Y. Gelfgat: *Magnetohydrodynamics*, 2015, vol. 51, no. 4, pp. 757-770.  
285 25. M. Ščepanskis, E. Yu. Koroteeva, V. Geža, A. Jakovičs: *Magnetohydrodynamics*, 2015, vol. 51, no. 1, pp. 37-44.

286 **List of figure captions**

- 287 Fig. 1 – attenuation coefficients for X-rays (150 keV) and thermal neutrons for different atoms
- 288 Fig. 2 - Design of a rectangular permanent magnet stirrer: (a) the drawing and the illustration of the flow pattern; (b) 3D rendering of  
289 the active part of the set-up.
- 290 Fig. 3 - The summary of different flow patterns as the result of different magnet rotation schemes.
- 291 Fig. 4 - Snapshots of neutron radiography visualization of the different type MHD flow (see designation in Tab. 2) at two different  
292 magnet rotation speeds: 7.05 rps and 21.15 rps.
- 293 Fig. 5 - Snapshots of neutron radiography visualization of the flow at different liquid levels (see designation in Tab. 2), magnet  
294 rotation speed 21.15 rps.
- 295 Fig. 6 - Snapshots of neutron radiography visualization of non-wetted particles in the A0 case (see designation in Tab. 2) for different  
296 magnet rotation speed.
- 297 Fig. 7 - An example of the results of premature image processing: (a) for the basic particles ( $0.3\pm 0.1$  mm); (b) for the large  
298 ( $>0.4$  mm). The raw neutron images are shown in the left column, and the proper processed images of the liquid metal zone  
299 are shown in the right column.
- 300 Fig. 8 - Examples of neutron PIV: (a) instant capture; (b) time averaged for 10 frames (0.31 s). These PIV images corresponds to A0  
301 rotation scheme, magnets rotation speed 28.2 rps.
- 302 Fig. 9 - An example of PTV post-processing: (a) illustration of particles identification by the algorithm (circles), the image  
303 corresponds to prematurely processed image in Fig. 7 (b raw); (b) particles trajectories calculated by the PTV algorithm.  
304 Large particles ( $>0.4$  mm), A0 magnets rotation scheme, 28.2 rps.

305 **Table I. Parameters of the set-up for solid particles – liquid metal flow visualization. See Fig. 2 (a) for**  
 306 **designations.**

Parameter	Value
$B_r$	1.3 T
$\omega$	7.05-35.25 rps
$D$	30.0 mm
$L_m$	50.0 mm
$b$	50.0 mm
$a$	21±2 mm*
$s$	0±1 mm*
$l$	100.0 mm
$h$	100.0 mm
$L_b$	30.0 mm

307 \* Parameters  $a$  and  $s$  contain errors since they are only hand adjusted dimensions, while all other distances and sizes are  
 308 machined with high precision (less than 0.1 mm)

309